AIAA JOURNAL
Vol. 34, No. 12, December 1996

Cold Gas Simulation of a Solid Propellant Rocket Motor

D. Couton,* F. Plourde,† and S. Doan-Kim‡
Centre National de la Recherche Scientifique, 86960 Futuroscope, France

The objective of this study is to characterize experimentally the mean and fluctuating flowfield and the dynamic instabilities that develop along a two-dimensional channel with porous walls. The channel is a $\frac{1}{40}$ scale model of the ARIANE 5 segmented solid rocket motor. This cold gas simulation is based on an aeroacoustic similitude that reproduces the Strouhal and Mach numbers and the complex internal geometry (obstacles, flowing cavity, submerged nozzle) of the full-scale motor. Measurement data, mean and fluctuating velocities, and shear stresses were obtained using a two-component laser Doppler anemometer. The injection wall, composed of a sintered Poral and of a metallic weaved sieve, gave a uniform injection velocity, with a controlled injected turbulence intensity. The second obstacle divided the flowfield into two regions. Upstream, the flow was laminar. A shear layer developed at the top and in the wake of the obstacle because of the interaction of the upstream main flow with the downstream injected flow. Downstream of the obstacle, velocity fluctuations increased and the shear layer became turbulent.

Nomenclature

a	= sound velocity
f	= characteristic frequency
h_c	= nozzle height
h_v	= channel height
I_t	= rms value, $\sqrt{(\overline{u'^2} + \overline{v'^2})}$
$I_{t\max}$	= maximum rms value at fixed x
L	= channel length
l	= channel width
M	= Mach number, u/a
$\dot{m}$	= mass flow rate
P_{fav}	= head-end pressure
Re_c	= Reynolds number based on u_c, $u_c h_v/\nu$
Re_o	= injection Reynolds number, $v_o h_v/\nu$
Sr	= Strouhal number, $f h_v/u$
T	= ambient temperature
U	= normalized velocity, u/u_x
u	= mean velocity in x direction
u_c	= maximum velocity of u
u_x	= mean velocity at fixed x, $(1/h_v)\int_0^{h_v} u(x, y)\,dy$
u'	= fluctuating velocity in x direction
$\overline{u'v'}$	= Reynolds shear stress
V	= normalized velocity, v/v_o
v	= mean velocity in y direction
v_o	= injection velocity
v'	= fluctuating velocity in y direction
X	= normalized coordinate along, x/L
x, y, z	= coordinates along, transverse, and lateral to the porous wall, respectively
Y	= normalized coordinate transverse, y/h_v
Z	= normalized coordinate lateral, z/l
γ	= specific heat ratio
ν	= kinematic viscosity
ρ	= density
σ_v	= local injection turbulence intensity, $\sqrt{v'^2}/v$
ϕ	= characteristic porous size

Received April 7, 1995; revision received March 5, 1996; accepted for publication Aug. 23, 1996; also published in *AIAA Journal on Disc*, Volume 2, Number 1.

*Engineer, Department of Energetics, Laboratoire d'Etudes Thermiques, Unité de Recherche Associée 1403, BP 109 Cedex.

†Doctor, Department of Energetics, Ecole Nationale Superieure de Mecanique et d'Aerotechnique, Laboratoire d'Etudes Thermiques, BP 109 Cedex.

‡Professor, Fluid Mechanics, Laboratoire d'Etudes Thermiques, Unité de Recherche Associée 1403, BP 109 Cedex.

Introduction

FOR some decades, solid rocket motors have become more and more powerful. For instance, each solid propellant booster of ARIANE 5 [solid rocket motor (SRM) P230] will develop a thrust of 7500 kN. It needs 238×10^3 kg of solid propellant, inside a 26-m-long booster. Three blocks of propellant are present in the motor, giving a segmented combustion chamber. This segmentation induces certain significant discontinuities in the internal geometry. Each block is separated from the other one by thermal protection. During solid propellant combustion, the regression of the burning surface reveals these thermal protections that become obstacles to the hot burnt gas flow. It is believed that there exists a potentially severe risk of hydrodynamic instabilities developing downstream of the obstacles. Segmentation produces regions of highly sheared mean flow, due to port area discontinuities and protrusions of inhibitor rings; in particular, a shear layer develops in the obstacle wake. Interaction between the instability of mean flow shear layer and acoustic motions in the chamber can occur. U.S. experience shows with segmented motors (namely the Space Shuttle and Titan solid boosters) that significant pressure and thrust oscillations happened during flight at the first axial mode frequencies. Experimentally, it is difficult to determine the characteristics of the internal flow with direct measurement due to the high temperature (3300 K), the pressure (4.6 MPa), and the velocity of the gases.

Meanwhile it is possible to obtain experimental information by means of a cold-flow model of the actual motor. Therefore, a $\frac{1}{40}$ scale model of the ARIANE 5 solid propellant rocket motor has been designed using an unsymmetrical porous-walled channel with complex internal geometry (cavities, obstacles, submerged nozzle), for a high-injection Reynolds number. Characteristic dimensions of the experimental apparatus have been determined by an aeroacoustic similitude with the full-scale motor. This similitude is based on the acoustic instability of the shear layer. The conservation of the Strouhal number, corresponding to the characteristic dimensionless acoustic frequency of the chamber, implies necessarily the reproduction of the value of the internal flow Mach number.

The present paper deals with injection-induced flow in a porous-walled rectangular channel. Many studies on this topic have been conducted over the last 50 years either analytically,[1–3] numerically,[4] or experimentally.[5–7] These studies have been performed with a two-dimensional or cylindrical channel with no discontinuities of geometry, like obstacles or cavities. The injected flow was obtained either at the head-end or along the duct. As for most experimental studies, our study was conducted with dry air. The injection was produced along the channel through a porous wall that was composed of a Poral made of sintered bronze spheres and a flexible metallic weaved sieve. The injection system is presented in detail in the description of the apparatus. The wall injection flow behavior is relatively well known in the case of a simple geometry (duct or planar

channel) without any discontinuities. The experimental results are in good agreement with analytical laws. Laminar velocity profiles can be adapted to many problems even if the values of the injection Reynolds number and the turbulence levels become significant. Nevertheless, transition from a laminar to a turbulent regime can occur. Transition can be reasonably well located by numerical approaches, for instance by implicit Navier–Stokes procedure,[8] but the turbulence intensity downstream of the transition location cannot be well predicted. Sabnis et al.[8] obtained numerical turbulence intensity levels two or three times higher than the experimental data. The transition process of important injection regimes has been studied, and a transition criterion based on the normalized surface pseudoturbulence parameter at the injection wall has been proposed by Beddini.[4] This parameter depends naturally on the injection Reynolds number Re_o and on dynamic injection conditions of the wall. Actually, it is assumed that jet coalescence occurs infinitesimally close to the injection surface and initiates nonnegligible fluctuation values in this area. This phenomenon causes increased turbulence levels in all of the flow inside the chamber.

The aim of the present study is to understand the behavior of the complex flow inside the chamber. For this purpose, it is essential to analyze the pattern of the flow upstream and downstream of the obstacle, and more precisely of the shear layer generated by the collision of the upstream main flow with the injection flow coming from the porous wall downstream of the obstacle. The presentation of the experimental apparatus shows its complex internal geometry, and different technical investigations are described. A particular emphasis is given on the wall injection conditions through porous surfaces; the use of both Poral and flexible weaved sieve provides good representative boundary conditions. The next part concentrates particularly on the mean flow pattern that emphasizes the position of different areas linked to the second obstacle position. An analysis of the experimental data concerning turbulence levels is proposed for the characterization of the growth and the development of the shear layer downstream of the obstacle. It allows us to make an estimation of the influence of the specific geometry on the flow behavior, on the instabilities of the shear layer, and on the collision of the main flow with the wall injection in this area.

Experimental Apparatus and Techniques

Test Channel

The experimental apparatus is composed of an unsymmetrical rectangular channel. The upper wall and the head-end are closed. The two side walls made of transparent glass allow visual access inside the channel, particularly to make laser Doppler anemometer (LDA) measurements and to visualize vortex structures downstream of the obstacle. Inside the chamber, the complex geometry is modular and presents certain discontinuities. These enable the characterization and the three-step simulation of the full-scale booster's operation: the first step corresponds to the beginning of the launching just after ignition and supposes that no propellant has yet burned; the second step corresponds to 50%, and the third characterizes 75% of web burnback. The present results were obtained with this last configuration shown in Fig. 1, called end of combustion.

The channel is 0.623 m long and 0.050 m wide. Injection occurs through three injection blocks. In the present configuration, the first block is not fed by air, because it represents the ignition segment, which burns rapidly. The injection block length is approximately $2L/5$, and the height of the channel (h_v) is 0.036 m. Each block is separated from the other by a cavity $L/31$ long whose height is close to $7h_v/6$. This cavity is similar to a sharp widening with an injecting wall. At the extremity of the cavity is located a protuberant obstacle, which gives locally an $h_v/2$ channel height. The rear end of the channel is connected to a submerged nozzle. The nozzle height is variable, regulating the different Mach numbers inside the chamber. The flow is sonic at the throat of the nozzle, ensuring acoustic isolation of the internal channel. The scale model does not reproduce the actual SRM geometry, but the scale model is roughly similar to a full-scale chamber, particularly obstacles, front injection, and discontinuities between the segmented blocks and submerged nozzle. Air at ambient temperature is injected through the porous walls. The uniformity of the mass flow rate distribution along the porous walls will be given further on. The airflow is supplied by a medium capacity blower to the plenum chamber, through storage tank, oil and water filters, and pressure reducers (Fig. 2). The maximum air outflow of the blower is a 0.083-m^3/s gust, and 0.055 m^3/s in steady state (normal conditions), equivalent to 0.065 kg/s under 0.18-MPa head-end pressure. Airflow is fed into a general manifold and divided into a number of flexible polyamide tubes. Different sonic air inlets are located between the distributor and each flexible tube, aiming at producing a constant mass flow rate in each injection cell.

Experimental Conditions

The aim is to reproduce the real flow of ARIANE 5 SRM when 75% of the propellant is burnt, so that the Strouhal and the Mach numbers have been preserved. The Strouhal number has been

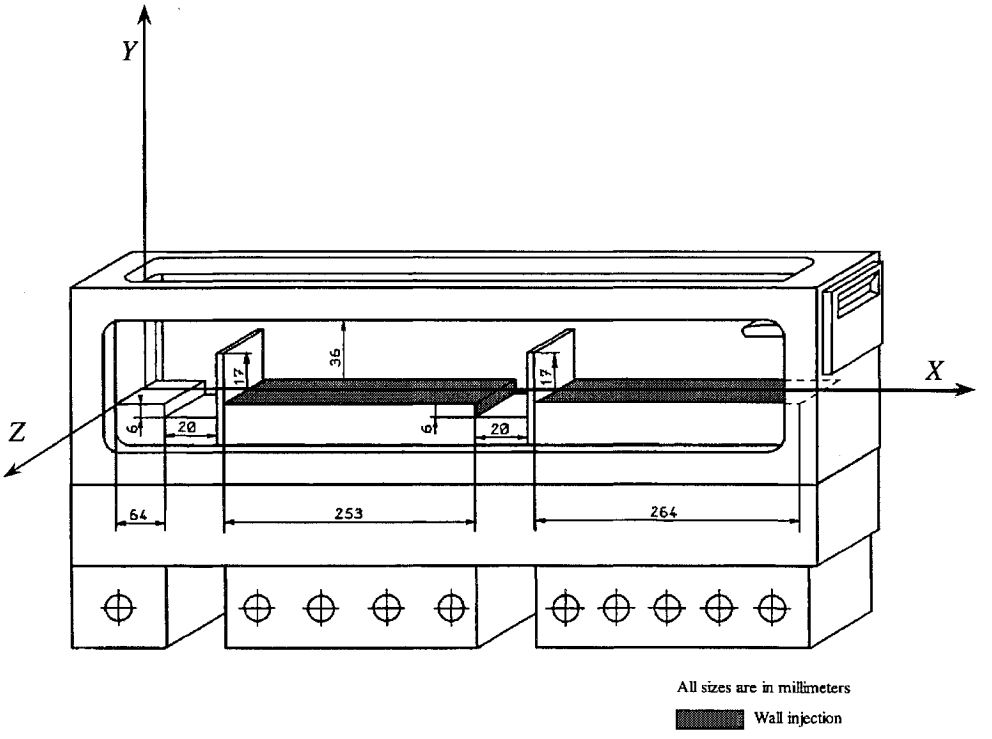

Fig. 1 Experimental configuration.

Table 1 Experimental conditions

	Full-scale P230	$\frac{1}{40}$ scale model
P_{fav}	46×10^5 Pa	1.83×10^5 Pa
$\dot{m}$	10.21 kg · s^{-1} · m^{-2}	2.50 kg · s^{-1} · m^{-2}
h_c	0.4475 m (radius)	3.08×10^{-3} m
h_v	1.425 m (radius)	36×10^{-3} m
γ	1.143	1.400
T	3442 K	298 K
M	0.050	0.050
Sr	0.570	0.570
Re_o	1.58320×10^5	4.920×10^3
Re_c	3.761630×10^6	7.15×10^4

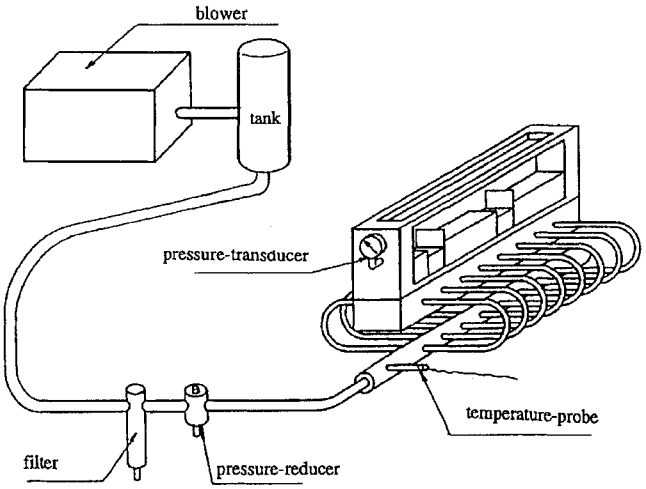

Fig. 2 Experimental setup.

evaluated with the channel height h_v, the mean velocity in the whole channel, and the first acoustic mode ($f = 278$ Hz). The Mach number is defined with the mean conditions of the flow. The choice of the adequate nozzle height h_c determines the rate of the mass flow injected in the channel and the level of internal pressure at head-end (P_{fav}). All of the characteristics conditions are listed in Table 1.

Measurement Techniques

To measure nonintrusively the velocity components and turbulence values of the flowfield, the LDA technique was used. The channel height was sufficient to be able to perform the velocity measurements across the whole section. Seeding of the flow was provided by an aerosol of micronized droplets of about 5–10 μm, pulverized into the main flow manifold. The laser was an argon-ion laser capable of a 10-W total optical power, whereas a two-component fiber-optic LDA system was used for the velocity measurements. The dimension of each ellipsoidal measuring volume was about 45 μm long, 45 μm high, and 0.460 mm wide, the largest dimension being perpendicular to the direction of the flow, i.e., in the Z direction. A photomultiplier with a color separator converted into electrical signals the light scattered for a sampling of 4000 validated particles on each optical path crossing the measuring volumes. These signals were processed by two burst spectrum analyzers (BSA). The measurements were carried out in a coincidence mode. Most of the measuring data were obtained with a relatively high mean data rate of about 4.5 kHz, giving an accuracy of 1.5%. The BSA were monitored by a computer that gave in delayed time the mean axial X and transverse Y components of the velocity, the axial and transverse fluctuations of the velocity, and the shear stress. Particular attention was given to the verification of the two-dimensional behavior of the flow, i.e., in the X, Y plane. The spatial resolution used in transversal direction was 1 mm in the general case and 0.1 mm where velocity gradients became significant, particularly in the shear zones.

Injected air temperature in the channel was measured by a K-type thermocouple, with a 0.4-mm diam, positioned on the manifold. Internal pressure was obtained at the head-end with a low-pressure quartz piezoelectric transducer for dynamic and steady-state conditions.

Injection-Boundary Conditions

Both Poral and metallic weaved sieve were chosen to make the injection porous wall. Many experimental studies concerning solid rocket motor combustion simulation have used only Poral.[9] In the present case, a sintered-bronze spheres Poral was set inside the injection blocks. The Poral surface was 5 mm thick and had a 100-μm porosity. It provided acoustic isolation of the chamber opposite the upstream device of injection (manifold, flexible tubes, injecting blocks). Although sintered-bronze spheres seemed to give a more uniform injection velocity than sintered stainless steel shavings,[10] the velocity measurements show that uniformity was not obtained. The measurements were performed, with the nominal mass flow rate, on the whole porous surface in longitudinal direction, i.e., from $X = 0.136$ to 1.0, except in the flowing cavity, and close to the injection surface at $Y = 0.028$ and $Z = -0.3$, because of optical considerations. The mean injection velocity was close to 1.18 m/s, but fluctuation values were quite significant, and turbulence levels were over 25% downstream of the Poral.

To decrease this local turbulence intensity and to obtain a uniform pattern of injecting surfaces, a flexible metallic weaved sieve of 75 μm was placed at 10 mm upon Poral. The monitoring of uniformity was carried out downstream of the sieve surface. The mean injected velocity was 1.15 m/s. Fluctuating time velocity shows that the local injecting turbulence intensity was reduced by a factor of 8 against the Poral surface and reached about 3%. The metallic sieve Reynolds number, based on injected mean velocity v_o and the metallic sieve diameter, was about 6. There, the characteristic Reynolds number was smaller than the critical Reynolds number, obtained by Groth and Johansson,[11] which was about 40. Boundary aerodynamic conditions therefore seem to be unable to shed vortices downstream of the sieve. An optimal quality of the injection is obviously required for this kind of flow development. The use of both Poral and metallic weaved sieve has a major drawback. The coalescent effect of the oil seeding through the injecting surface, during laser anemometer measurement, requires the control of porous wall cleanness during data acquisition. Precautions were taken to assure that a uniform inflow condition was achieved.

Mean Flow Pattern

The end-of-combustion configuration has been the object of previous works.[12] The present work was conducted to analyze in detail complex flow behavior and its pattern upstream and downstream of the obstacle.

The internal flow can be considered as incompressible ($\Delta P/P \approx 1.7\%$) from the head to the entrance nozzle. Assumption of uniform injection velocity can be verified by computing the change of the mean velocity u_s vs the normalized axial position X. Figure 3 shows the increase of u_s, measured in an (X, Y) plane in the middle of the channel ($Z = 0.0$); 95 locations in the axial direction were used to describe the uniform mass flow rate distribution. Upstream of the flowing cavity and downstream of the obstacle, u_s increases linearly from 0.0 to approximately 18.5 m/s and is in agreement with the assumed uniform injection. Moreover, the mean velocity u_s does not change so regularly in the flowing cavity and at the obstacle passage because of the irregular geometry and the dynamic conditions in this area. In the flowing cavity, sharp increase of the passage height (17%) creates a mean velocity decrease. Similarly, at the obstacle

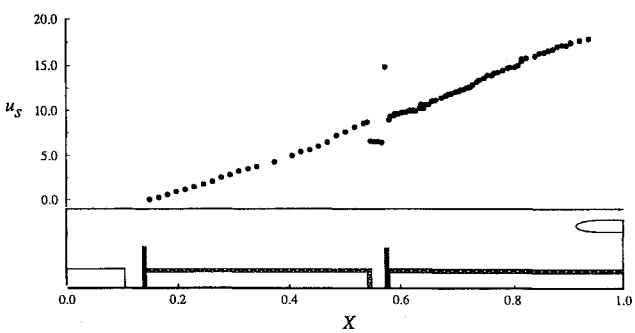

Fig. 3 Change of the mean longitudinal velocity u_s vs axial position X.

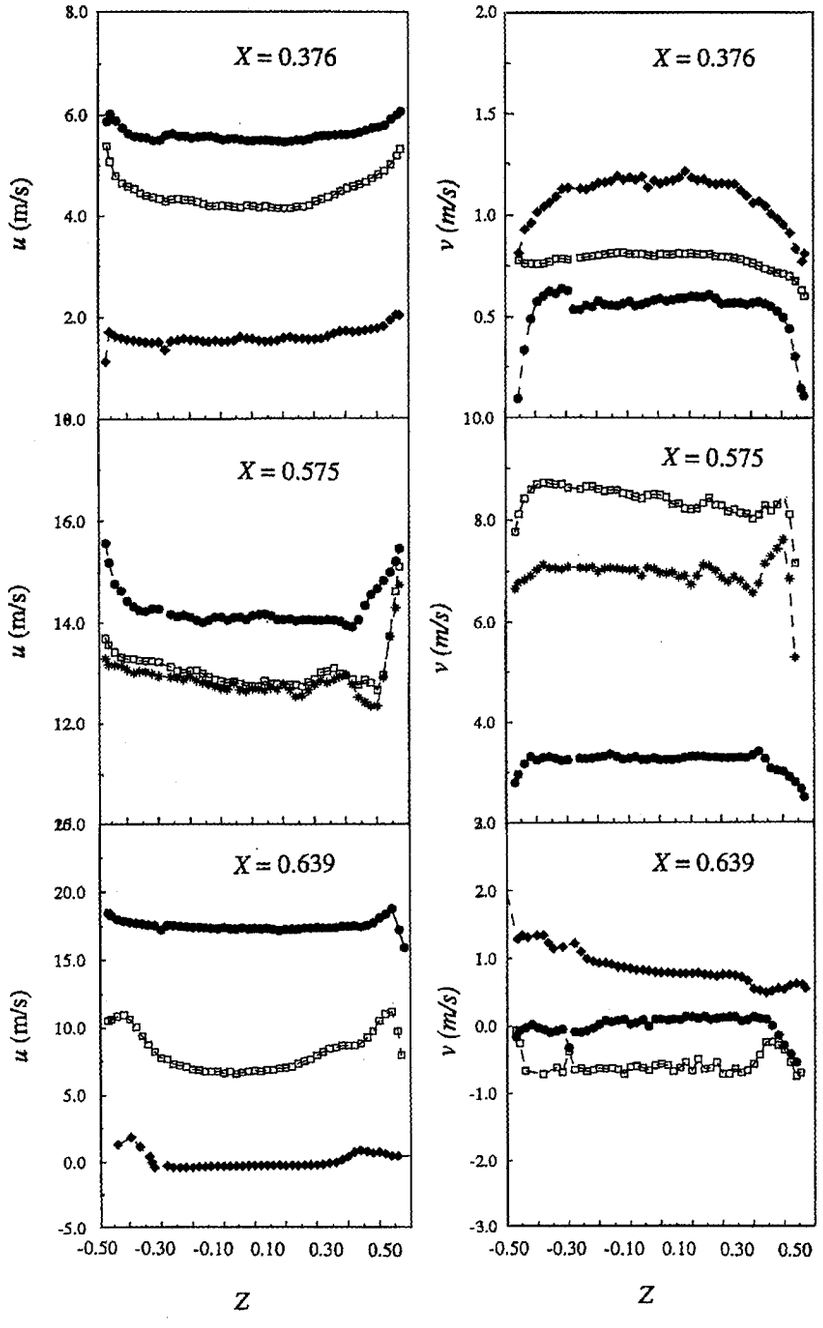

Fig. 4 Change of the mean velocity component (u, v) vs lateral position Z: ●, Y = 0.722; □, Y = 0.528; ∗, Y = 0.556; and ♦, Y = 0.167.

location, the sharp decrease of the passage height (47%) creates an acceleration of the mean velocity.

Simulation considerations generate that the present channel is longer than high or wide. In the studied configuration, the width to length ratio (l/L) is equal to 0.080 and the height to length ratio (h_v/L) to 0.058. Under such ratios, it is not obvious that the two-dimensionality of the flow is preserved. Therefore, the change in two-dimensional flow must be checked. Measurements of the two components u and v were made at different X, Y positions in lateral direction Z. Figure 4 shows the variation of the mean components of the velocity at $X = 0.376$, 0.575, and 0.639, i.e., respectively upstream, at, and downstream of the obstacle. The velocity measurements are obtained for different channel transversal positions of Y. In agreement with all of the lateral measurements, that u and v velocity components are roughly not affected by the lateral position Z and reach constant values at a given (X, Y) position, both near the injecting wall ($Y \approx 0.0$) and the upper window ($Y = 1.0$). Note that u and v are positive except at $X = 0.639$ and $Y = 0.528$, where the transversal velocity component is negative, close to −0.70 m/s, but not significant compared with u that reaches 7.6 m/s. The upstream main flow, which was accelerated at the obstacle position, meets with the downstream injecting flow. A recirculating zone would develop if there were no injection through the porous wall. Injecting flow influences the main flow and pushes the main flow in the upper area of the channel. At this location, the main flow is not quite parallel to the axial direction. Nevertheless, some disturbances are obtained close to the two glass windows, located at $Z = -0.5$ and 0.5, but for all of the measurements, constant values are observed for $-0.3 \leq Z \leq 0.3$. Behind the obstacle, profiles of longitudinal and transverse velocity components seem to be slightly more disturbed in this lateral direction than those obtained upstream of the obstacle. However, constant values for the longitudinal component as well as the transverse one confirm the assumption of two-dimensional flow organization.

Upstream of the obstacle, the flow organizes itself like a well-known wall injection flow. Figure 5 presents longitudinal and transverse dimensionless profiles at two different locations in this region. Normalization of the longitudinal component is through the mean velocity u_s, and that of the transversal component through the

injection velocity v_o. Near the injecting wall, V tends toward 1.0 and decreases when Y increases. In the upper window vicinity, U reaches its maximum value. Actually, the boundary layer on the upper window can be assimilated to boundary-layer development with a stagnation point on a flat plate, already noticed in Ref. 13. Dimensionless profiles are in good agreement with the analytical approach. Most of the experimental investigations on wall injection flow, either cylindrical or rectangular channel, reveal a similar change for the mean flow. Based on experimental evidence, Yamada et al.[6] prematurely concluded that laminar flow would persist for much greater axial Reynolds numbers. Nevertheless, Dunlap et al.,[5] Olson and Eckert,[14] or Avalon,[15] for instance, obtained experimentally a laminar turbulent transition. Beddini[4] characterized the transition phenomenon by showing the direct link between the transition and both the axial Reynolds number and the injection Reynolds number.

All of the works already mentioned were conducted as part of the studies on wall injection flow with no geometric discontinuities. Here with this flow the discontinuous geometry (obstacles) and the presence of a flowing cavity have been taken into account.

First, it is interesting that the flowing cavity has the same geometrical shape as a classical rear-facing step. The presence of forward flowing wall creates a secondary longitudinal flow and gives a specific configuration. There are then two different flow circulations with the same direction as shown in Fig. 6, a mixing layer being created by a significant velocity gradient between the main and the forward flow. The longitudinal and transverse velocity profiles are plotted in Fig. 7, the main flow longitudinal velocity being 10 times higher than the horizontal flow. Because of this ratio, the disturbances would have a tendency to develop perturbations inside the flowing cavity. Longitudinal profile shapes present different behavior and particularly a local maximum velocity at $Y = 0.15$ that is responsible for modifying the flow development out of this particular backward-facing step. This change can be explained by the cavity geometry, which favors the transverse flow acceleration. Visualization studies carried out previously[16] give a qualitative approach that confirms this pattern. In particular, no creation of vortex structures can be observed in the mixing layer of the flowing cavity. Moreover a counter-rotating eddy occurs more or less at the obstacle base. Even if the backward-facing step provides a particular geometry, disturbances are quite local and the presence of a protuberant obstacle prevents development of cavity disturbances.

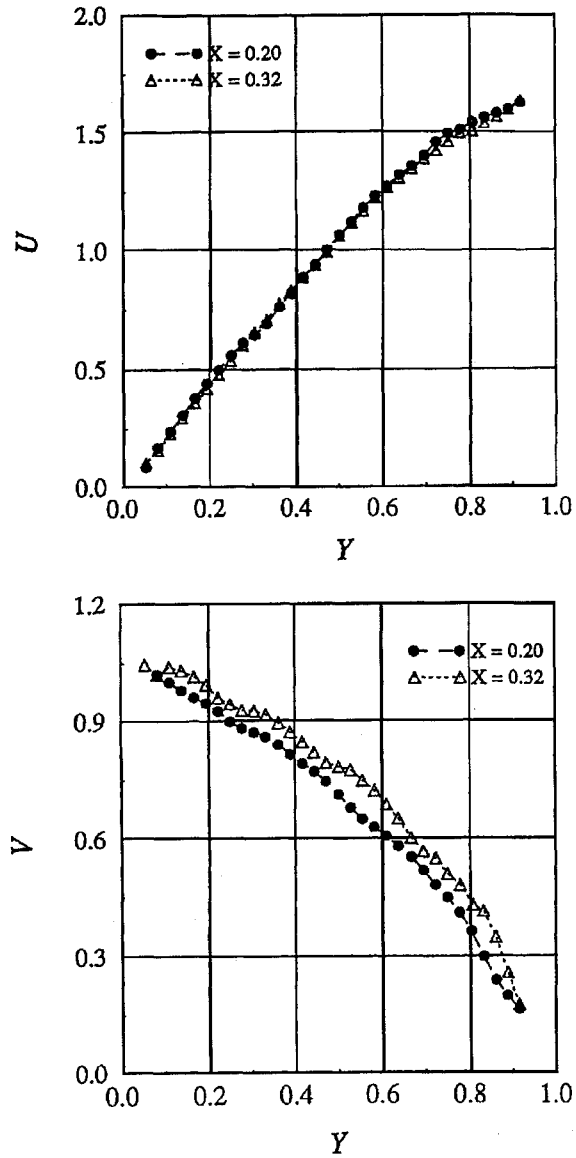

Fig. 5 Change of the mean velocity (U, V) vs Y upstream of the obstacle.

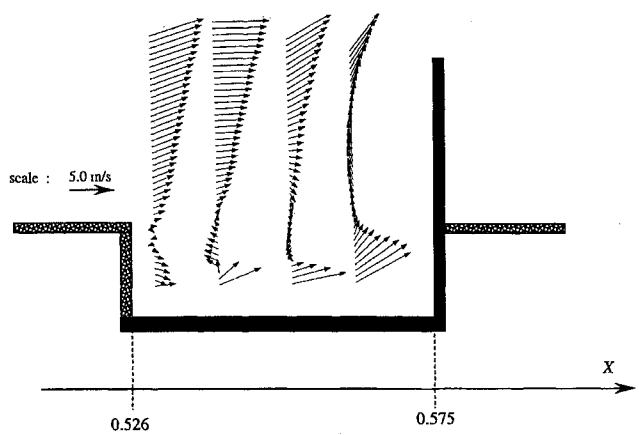

Fig. 7 Longitudinal and transverse mean velocity profiles vs Y in flowing cavity.

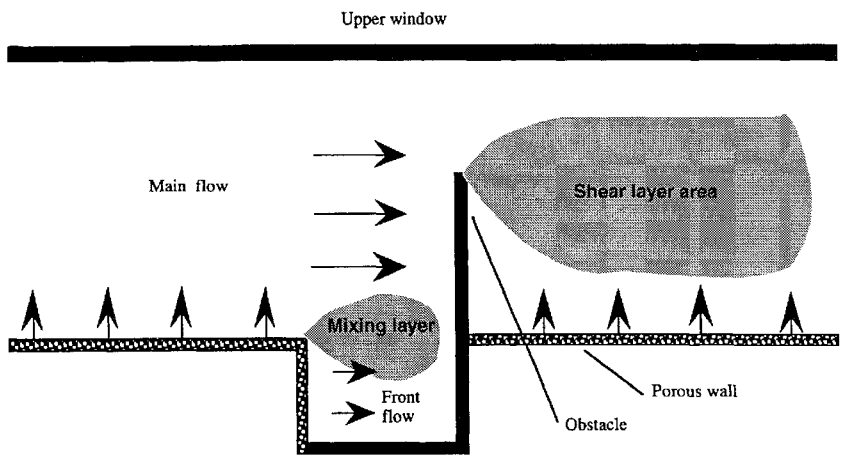

Fig. 6 Specific mixing layer development.

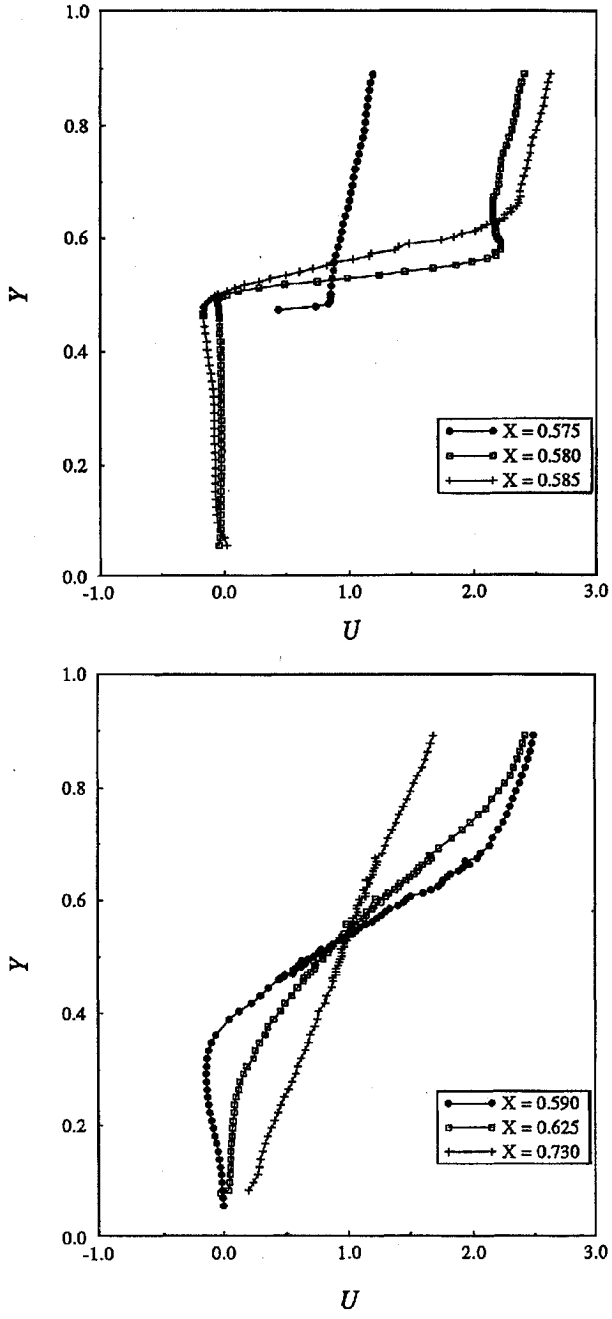

Fig. 8 Longitudinal velocity profiles downstream of the obstacle.

On the other hand, experimental velocity measurements made in the median plane ($Z = 0.0$) show dynamic disturbances of the flow behind the obstacle and more precisely in its wake. Longitudinal velocity profiles, plotted in Fig. 8, present two different flow pattern areas. The first is located directly at the obstacle position ($X = 0.575$) and stretches to $X = 0.585$, where the longitudinal component is divided in three transverse areas: 1) between the injection wall ($Y = 0.0$) and the top of the obstacle ($Y = 0.472$), the longitudinal velocity U is negative with a low amplitude; 2) immediately at the top of the obstacle, the flow is intensely sheared and presents dynamic instabilities; and 3) over this sheared area, longitudinal profiles seem to be undisturbed by the obstacle and represent the historical conservation of the upstream flow. The second longitudinal velocity area pattern is mainly characterized by the disappearance of negative U values and the rapid decrease of the longitudinal component transverse gradients.

Turbulence Development

The distributions of the rms value I_t upstream of the obstacle are presented in Fig. 9 for different axial locations. Only a few profile

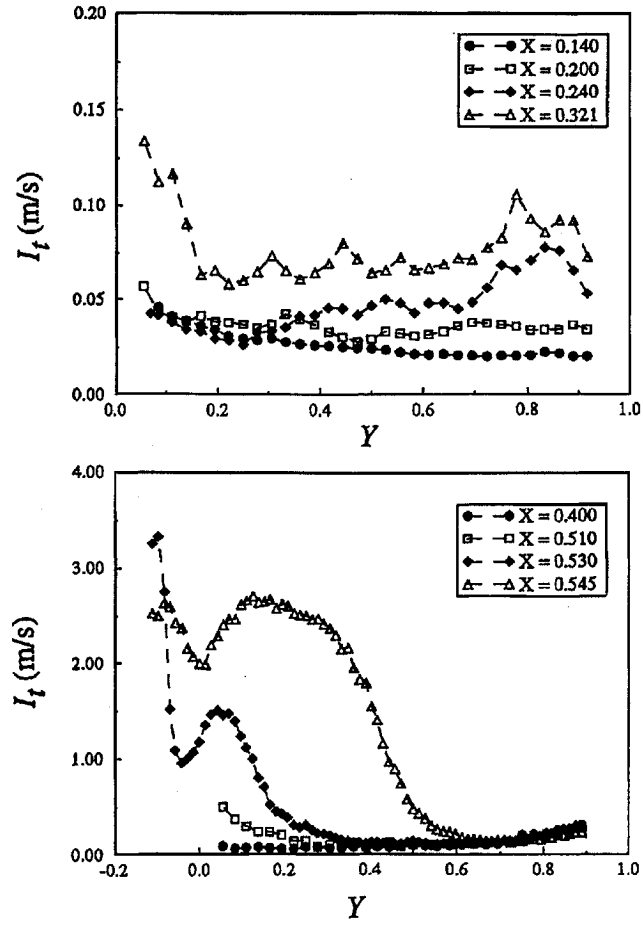

Fig. 9 Change of I_t upstream of the obstacle.

sections are plotted, but the results omitted do not change the layout. On the entire first part of the upstream region ($X \leq 0.575$), fluctuation values are very low ($I_{t\,\max} \leq 0.05$ m/s) representing just 1 or 2% of the mean longitudinal velocity u_s. When X increases, it can be observed that rms increases but less significantly. In the vicinity of the flowing cavity and the particular rear-facing step near the injecting wall ($Y = 0.0$), the turbulence I_t increases. But directly in the flowing cavity, fluctuation values are no longer negligible. In fact, the mixing layer, identified by the mean velocity, is turbulent: it develops rapidly because of the limited geometry characteristics. For example, at $X = 0.545$, two rms intensity peaks appear in the flowing cavity at $Y = -0.070$ and outside of the cavity at $Y = 0.100$. This axial profile shape develops substantially. The inner peak is strongly reduced, and at the same time, the outer peak becomes larger and higher. Turbulence activities propagate toward the main flow. Close to the location of the obstacle, significant fluctuation values fill the wall injection side. But, as we have already mentioned, the presence of a protuberant obstacle reduces significantly the passage area, thus creating a strong acceleration of the main flow. This prevents the propagation of the turbulence field, created in the mixing layer all along the channel and particularly in the downstream obstacle area. In fact, even if some disturbances are noticed because of the flowing cavity upstream of the obstacle, the flow is laminar.

The variation in the main turbulent quantities indicates the effect of the obstacle on the flow pattern.

The I_t distributions, obtained from axial measurement made at several locations, are presented in Fig. 10 (more than 5000 measurement points have been necessary for a good flow description). These results present high values in the obstacle wake. For instance, immediately above the top of the obstacle ($X = 0.575$), I_t reaches approximately 7 m/s. This maximum peak amplitude is very significant and represents, in fact, more than 50% of the mean longitudinal velocity at this location. Moreover, it can be observed that the I_t profile has inflexion points as do the longitudinal velocity profiles. The

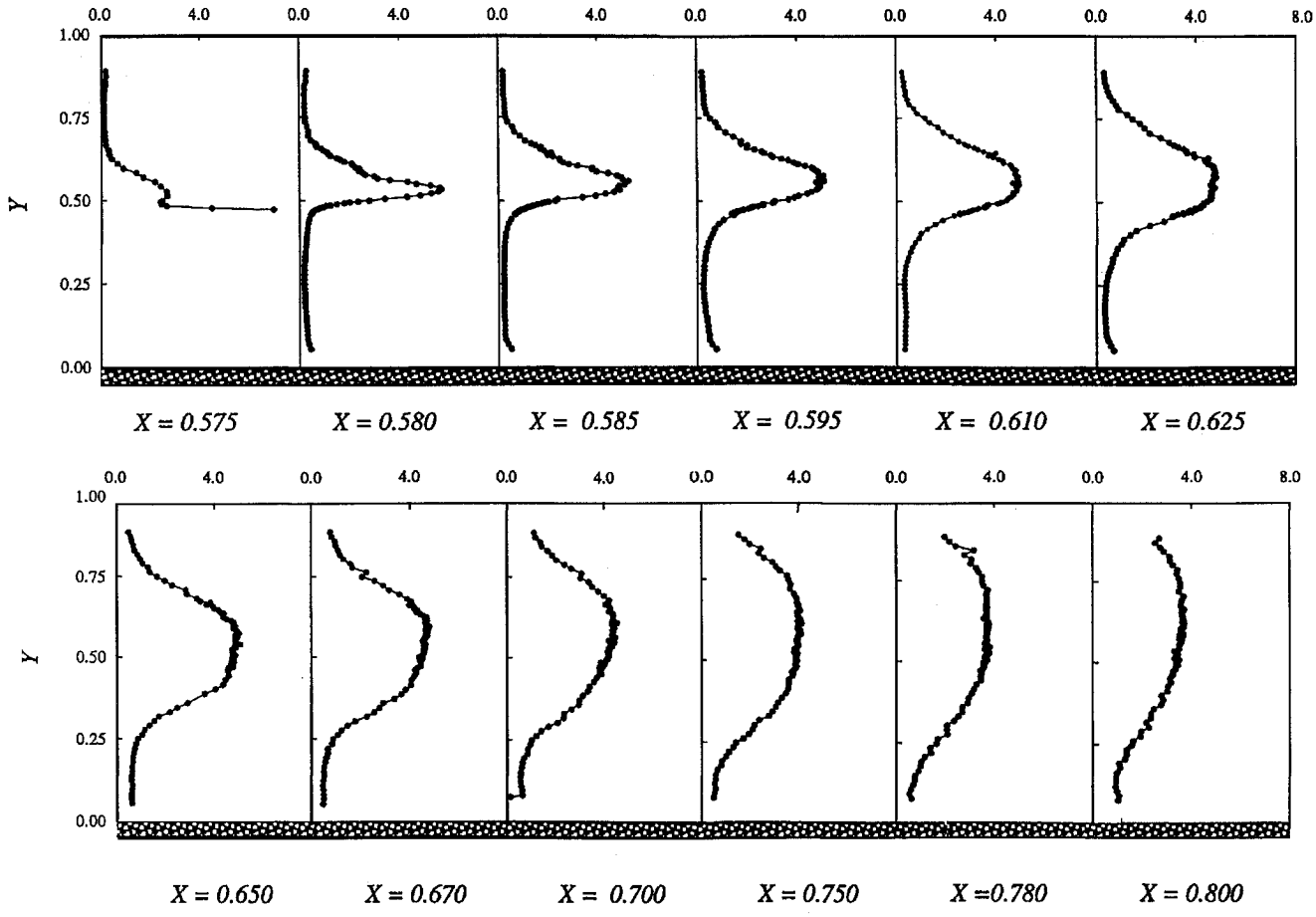

Fig. 10 RMS [I_t (m/s)] distribution downstream of the obstacle.

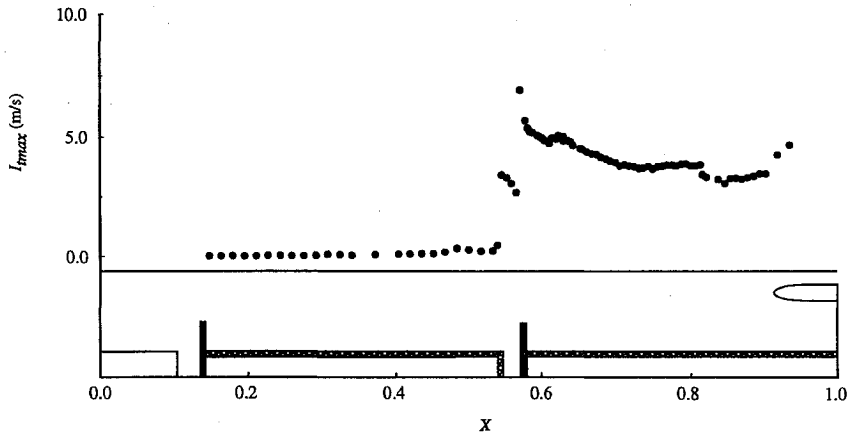

Fig. 11 Change of $I_{t\,\max}$ along the chamber.

downstream flow runs against the top of the obstacle, creating a detachment phenomenon, and a maximum of mass transfer occurs on a minimum thickness. The shear layer creates a much disturbed flow area with overspeed and inflexion points either on the mean distribution or on the turbulence quantities profile. This area plays a very important role in the development of the entire shear layer, because it corresponds to the origin of the shear layer and controls its stable or unstable development. Behind the obstacle, turbulence values always reach a maximum at the obstacle height ($Y = 0.50$). Fluctuation values upstream and downstream of the obstacle can be compared graphically in Fig. 11 by the variation of the maximum rms value $I_{t\,\max}$ vs the longitudinal position X. Downstream of the obstacle, $I_{t\,\max}$ is significant, decreases slightly when X increases, but always conserves a significant value ($I_{t\,\max} = 4$ m/s). Moreover, in the back-end region, i.e., in the vicinity of the submerged nozzle ($X \geq 0.948$), fluctuation intensity increases again. All of the works concerning flows induced only by wall injection are in agreement when concluding that this particular flow delays significantly the transition of a laminar flow from becoming turbulent. In the present case, a turbulence flowfield is created only because of the presence of strong viscous forces in the obstacle wake.

A complete description of turbulent behavior in the case of a nozzleless motor simulation without any geometric discontinuities has been given by Traineau et al.[7] Shear stress measurements were obtained by the LDA technique. The same technique has been used in our study. Shear stress $\overline{u'v'}$ profiles are plotted in Fig. 12 for different longitudinal X values downstream of the obstacle. Shear stresses start off strongly in the obstacle wake (Y close to 0.550). Maximum levels reach values of about 5–6 m^2/s^2, representing about 15% of the square mean longitudinal velocity at this location. The $\overline{u'v'}$

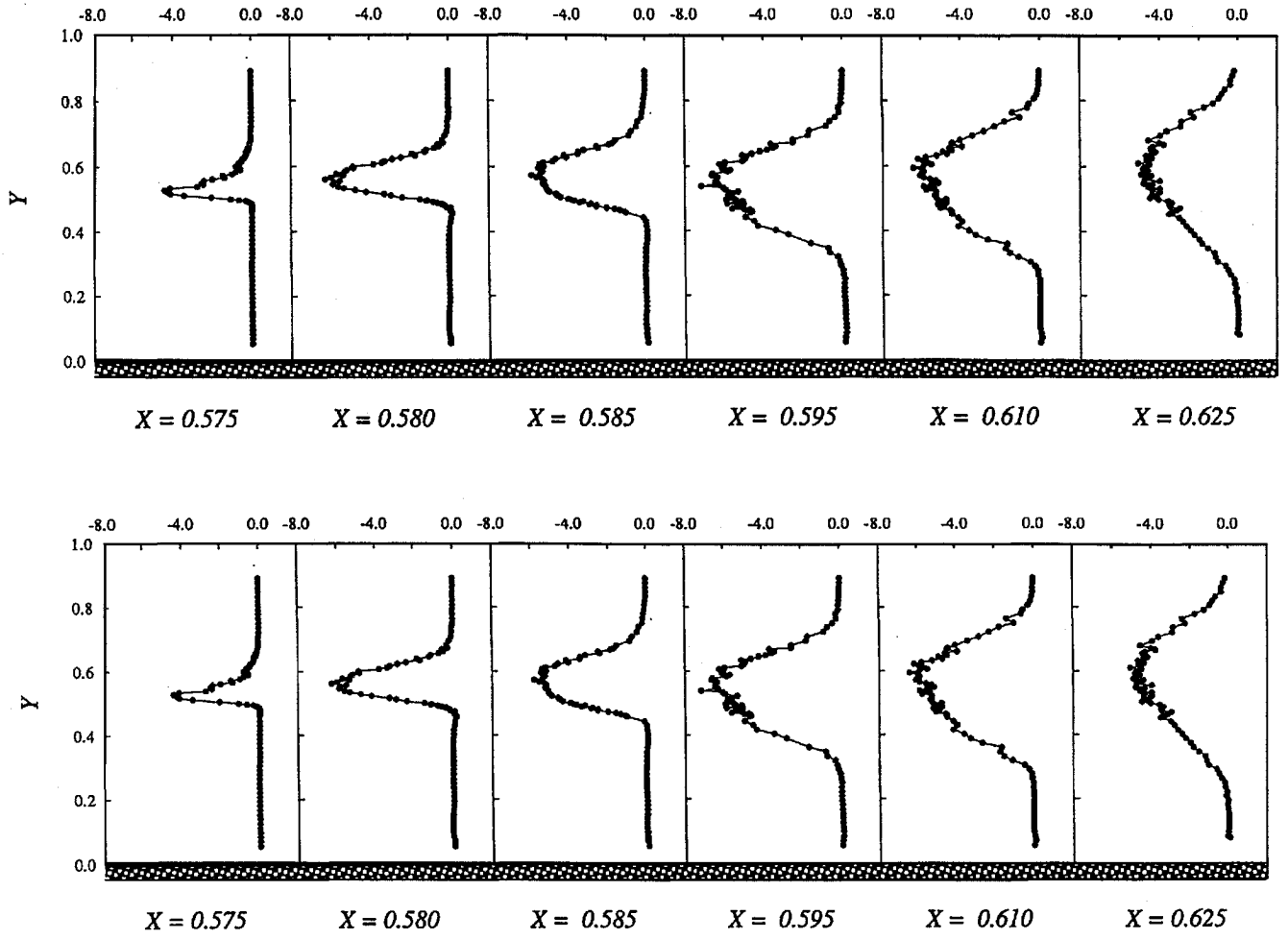

Fig. 12 Shear stress (m^2/s^2) profiles downstream of the obstacle.

profile shapes change in the same characteristics shape as I_t shapes. For instance, at $X = 0.580$, the shear stress profile presents a peak, and $\overline{u'v'}$ tends toward zero on both sides of the transverse position.

It can be noticed that turbulent calculations with a k-ε model[16] give profiles similar in shape and intensity to those obtained experimentally. This peak increases progressively in amplitude and particularly widens out. This means that the characteristic turbulence value stretches both on the sides of the main flow and on the injecting wall. However, turbulence diffusion is not symmetrical on both sides of the top of the obstacle transverse position. Between $X = 0.580$ and 0.690, turbulence diffusion is apparent toward the injecting wall, because of the significant convection wall flow, and at the same time, the large turbulence diffusion can be noticed in the main flow direction. Beyond $X = 0.690$, shear stress profiles become flatter and the turbulence activity spreads on all of the channel height. Characteristic turbulence intensity decreases as soon as X increases and describes a similar variation. Immediately in the vicinity of the porous plate, no particular change can be noticed. Actually, the injection conditions, which are controlled, do not create any significant turbulence value: this study shows that the injection system does not create any pseudoturbulence, particularly characteristic for this type of injection flow. With Re_o and Re_c levels, the flow would have laminar characteristics but geometric discontinuities precipitate it toward an intense turbulent flow. Turbulence characteristics are significant inside the shear layer. The rms of the longitudinal u' and transversal v' velocity fluctuations are presented in Fig. 13 at different longitudinal locations downstream of the obstacle. These quantities are normalized by the mean longitudinal velocity u_s. All of the behaviors that can be observed on these fluctuation shape profiles can, in fact, be already observed in the change of turbulence intensity and shear stress variation.

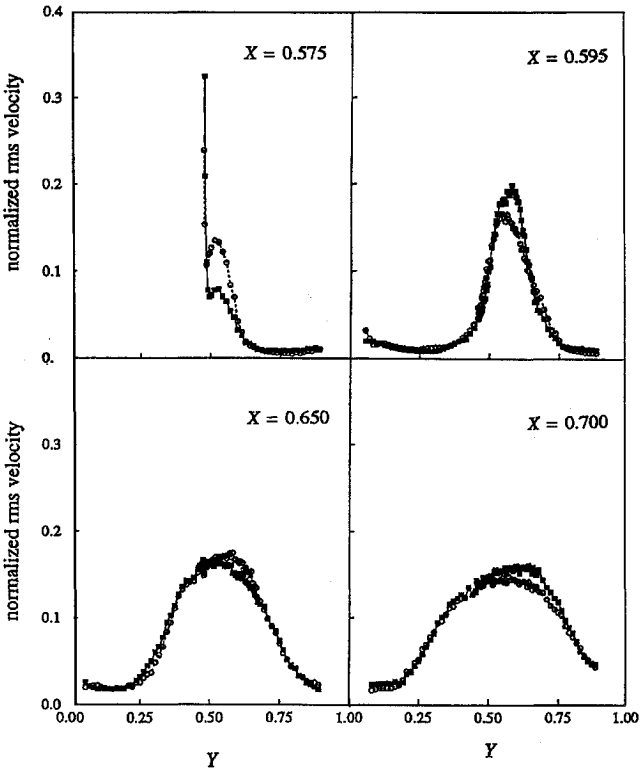

Fig. 13 Normalized $\overline{u'^2}$ and $\overline{v'^2}$ profiles: ○, $\sqrt{v'^2}/u_s$ and ■, $\sqrt{u'^2}/u_s$.

Moreover, a comparison between $\overline{u'^2}$ and $\overline{v'^2}$ variation in the shear layer shows there is a presence of turbulence homogeneity. For example, at $X = 0.575$, $\overline{u'^2}$ is greater than $\overline{v'^2}$, but the characteristic disturbed profile has the same change for the longitudinal and the transverse components. Turbulence profiles reach about 40% of the mean longitudinal velocity, but these values decrease when X increases. The rms of the longitudinal and of the transverse fluctuation velocities are similar. Beyond $X = 0.595$, the two turbulent profiles merge. Turbulence develops homogeneously in the shear layer.

Conclusions

We present here a simulative study on the injection-induced flows of a segmented solid propellant rocket motor. Experiments were performed using a rectangular channel with porous wall, through which air at ambient temperature was fed. Mean and fluctuating flowfield velocities and turbulence intensity were obtained with the LDA technique.

The injection turbulence value was significant behind bronze Poral and decreases by 8 behind a metallic weaved sieve to reach 4%. This particular low value characterizes good injection boundary conditions. The complex internal geometry reproducing a full-scale motor was composed of injection blocks, cavities, submerged nozzle, and obstacles that disturbed flow development. A two-dimensional flow was verified all through the channel. Upstream of the second obstacle, velocity profiles were characterized by cosine type and the turbulence level was lower than 2%: the flow regime was laminar. The term I_t increased in the injecting cavity because of the protuberant obstacle. Full flow development was disturbed by the obstacle, which accelerated the upstream flow. Similarly, flow was injected behind the obstacle. The collision of the two flows was localized at the top of the obstacle and generated a sheared flow development. The maximum value of turbulence intensity in the wake of the obstacle corresponded to a sheared flow where shear stresses exceeded 15% of the mean longitudinal velocity. Further back of the obstacle, turbulence level decreased slightly, and the mean flow pattern was completely modified.

This study presents a particular shear layer development, created in the wake of an obstacle in a channel with porous wall mass transfer. Future study of this complex flow will involve assessment of the stability of the shear layer. Further steps will also contribute towards the study of the coupling phenomenon between dynamic instabilities with an acoustic flowfield. The final objective of this study is to characterize experimentally the vortex shedding phenomenon.

Acknowledgments

This research was sponsored by the Centre National d'Etudes Spatiales. We give special thanks to R. Bec and E. Robert. Studies were scheduled under a cooperative research program of the ONERA dealing with ARIANE 5 segmented solid propellant motor stability prediction.

References

[1]Taylor, S. G., "Fluid Flow in Regions Bounded by Porous Surface," *Proceedings of the Royal Society of London*, 234A, 1199, 1956, pp. 456–475.

[2]Berman, S. A., "Laminar Flow in Channels with Porous Wall," *Journal of Applied Physics*, Vol. 14, No. 9, 1953, pp. 1232–1235.

[3]Yagodkin, V. I., "Use of Channels with Porous Walls for Studying Flows Which Occur During Combustion of Solid Propellant," *Proceedings of the 18th Aeronautics Congress*, Vol. 3, 18th Aeronautics Congress Symposium (Moscow), 1967, pp. 69–79.

[4]Beddini, A. R., "Analysis of Injection Induced Flows in Porous Walled Duct with Application to Aerochemistry of Solid Propellant Motor," Ph.D. Thesis, Graduate Program in Mechanical and Aerospace Engineering, Rutgers Univ., New Brunswick, NJ, Oct. 1981.

[5]Dunlap, R., Willoughby, P. G., and Hermsen, R. W., "Flow Field in a Combustion Chamber of a Solid Propellant Rocket Motor," *AIAA Journal*, Vol. 12, No. 10, 1974, pp. 1440–1442.

[6]Yamada, K., Goto, M., and Ishikawa, N., "Simulative Study on the Erosive Burning of Solid Rockets Motors," *AIAA Journal*, Vol. 9, No. 14, 1976, pp. 1170–1176.

[7]Traineau, J. C., Hervat, P., and Kuentzmann, P., "Cold Flow Simulation of a Dimensional Nozzleless Rocket Motor," AIAA/SAE/ASME 22nd Joint Propulsion Conf., Huntsville, AL, 1986.

[8]Sabnis, J. S., Gibeling, H. J., and McDonald, H., "Calculation of Solid Propellant Rocket Motor Internal Flow Field Using an Implicit Navier–Stokes procedure," AIAA 18th Fluid Dynamics and Plasma Dynamics and Lasers Conf., Cincinnati, OH, July 1985.

[9]Dunlap, R., Blackner, A. M., Waugh, R. C., Brown, R. S., and Willoughby, P. G., "Internal Flow Field Studies in a Simulated Cylindrical Port Rocket Chamber," *Journal of Propulsion*, Vol. 6, No. 6, 1992, pp. 690–704.

[10]Heaman, J. P., Ramachandran, N., Smith, A. W., and Yeh, Y. P., "Injection Induced Flow from Porous Medium in Cold-Flow Simulation of Solid Rocket Motors," AIAA/ASME/SAE/ASEE 30th Joint Propulsion Conf., Indianapolis, IN, June 1994.

[11]Groth, J., and Johansson, A. V., "Turbulence Reduction by Screens," *Journal of Fluid Mechanics*, Vol. 197, 1988, pp. 139–155.

[12]Plourde, F., Poisson, R., and Doan Kim, S., "Turbulence and Mass Transfer in a Segmented Flow with Wall Injection—Geometry Influence," *International Symposium on Turbulence, Heat and Mass Transfer*, Vol. 1, International Centre for Heat and Mass Transfer, Lisbon, Portugal, 1994, pp. 241–246.

[13]Plourde, F., Poisson, R., and Doan Kim, S., "Experimental Study of a Segmented Flow with Wall Injection," *4th Triennial International Symposium on Fluid Control, Measurement, and Visualization* (Toulouse, France), Vol. 2, 1994, pp. 817–822.

[14]Olson, R. M., and Eckert, E. R. G., "Experimental Studies of Turbulent Flow in a Porous Circular Tube with Uniform Fluid Injection Through the Tube wall," *Journal of Applied Mechanics*, Vol. 33, 1960, p. 817.

[15]Avalon, G., "Aérodynamique interne des propulseurs à propergol solide," ONERA, Internal Rept. 4/2486EY, Chatillon, France, Dec. 1991.

[16]Plourde, F., "Structures turbulentes d'un écoulement segmenté à injection pariétale," Ph.D. Thesis, Dept. of Energetics, Univ. of Poitiers, France, Nov. 1994.